Assessing flow liquefaction triggering considering fabric anisotropy effects under the ACST framework

Srinivas Vivek Bokkisa[a], Jorge Macedo[a,*], Alexandros L. Petalas[b], Chloé Arson[a]

[a]*School of Civil and Environmental Engineering, Georgia Institute of Technology, Atlanta, GA, United States*
[b]*Department of Engineering, Durham University, Durham, UK*

Abstract

Previous experimental studies have shown that the onset of instability in sands under undrained loading is affected by the initial state (i.e., void ratio and confinement), intermediate stresses, and fabric anisotropy. These experimental results have motivated numerical studies that investigate the conditions for instability triggering; however, most efforts have been focused on triaxial conditions, mainly addressing the role of state with few notable exceptions that extend to a multiaxial setting incorporating fabric anisotropy. In this study, we use the relatively new anisotropic critical state theory (ACST) to investigate the onset of instability in sands under undrained loading considering the role of state, multiaxial loading, and fabric anisotropy. We use the ACST-based SANISAND-F constitutive model to extend a previously established stability criterion and take into account the effect of fabric anisotropy in a multiaxial setting. The analytical instability criterion is derived from the fabric-dependent constitutive equations, and predicts the plastic modulus and the flow stress ratio at the instability point. The derived criterion highlights the benefits of the ACST framework to incorporate fabric and anisotropy effects. Lastly, we show that the stress ratio at the instability onset is not significantly affected by the extent of anisotropic consolidation.

Keywords: Flow liquefaction, Instability criterion, SANISAND-F, Fabric, fabric anisotropy, Anisotropic critical state theory, Anisotropic consolidation

*Corresponding author
Email address: jmacedo3@gatech.edu (Jorge Macedo)

1. Introduction

The onset of instability under monotonic loading of granular materials, also referred to as static liquefaction or flow liquefaction, has caused numerous geotechnical failures in the past (Bjerrum, 1971; Castro, 1969; Fourie et al., 2001; Hazen, 1918; Jefferies and Been, 2019; Morgenstern et al., 2015, 2016; Muhammad, 2012; Olson, 2001). Flow liquefaction is associated with a state of instability followed by sudden increases in strain and pore water pressure. It can occur in any saturated or near-saturated contractive soils, such as very loose sands, silts, as well as very sensitive clays. Previous research has suggested that the instability onset triggers at a characteristic stress ratio. This concept is illustrated in Figure 1 using undrained triaxial tests from Lade (1999). In particular, Lade (1999) highlighted that the stress state at the point of instability for samples with the same initial density but under different confining stresses are aligned on a unique line called the instability line. This so-called instability line represents the stress conditions in which flow liquefaction triggers leading to the potential instability region shown in Figure 1.

Experimentally, flow liquefaction has been mostly explored under triaxial conditions (Ishihara, 1993; Konrad, 1993; Sladen et al., 1985). Previous research has shown that despite some small differences in the definitions adopted and conclusions drawn, physical interpretations are consistent across different studies, i.e., the instability onset specifies a yielding point where large plastic strains can develop (Chu et al., 2003; Lade, 1993; Najma and Latifi, 2017). The effect of initial anisotropy (induced during consolidation before shearing) under triaxial conditions has also been subject to different interpretations. For example Najma and Latifi (2017) used undrained triaxial compression tests on Sacramento sands performed by Kramer (1996) and suggested that the higher the anisotropy during initial consolidation, the steeper the slope of the instability line. In contrast, Kato et al. (2001) using anistropically consolidated specimens of Toyoura sand subjected to undrained triaxial compression loading, suggested that the slope of the instability line did not vary significantly with respect to the initial anisotropic consolidation. Beyond the triaxial conditions, Chu and Wanatowski (2008) performed plane strain tests on Changi sand to understand the

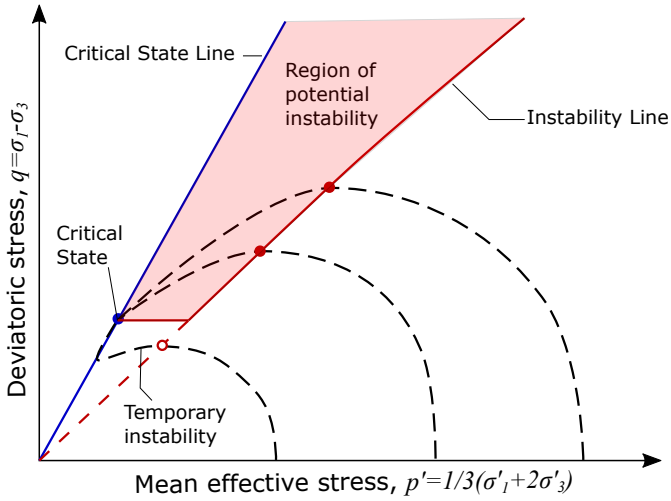

Figure 1: Illustration of instability line in a $p' - q$ space, considering undrained triaxial compression tests. Modified from Lade (1999). p' represents the mean effective stress and q the deviatoric stress. Temporary instability refers to the condition where there is a reversal in the stress path towards the critical state. The shaded region marks the potential instability region.

conditions for flow liquefaction. An instability line was established, which was dependent on the state parameter defined by Been and Jefferies (1985). Chu and Wanatowski (2008) also suggested that a normalization of the instability stress ratio (η_f) by the stress ratio at the critical state (M) provides a unique relationship in terms of the initial state parameter. Using this relationship, the instability conditions established under triaxial conditions can be used for plane strain conditions if M is known.

Other studies have also highlighted the role of the rotation of principal stress axes and the magnitude of the intermediate stress on the onset of flow liquefaction. For example, Yoshimine et al. (1998), Georgiannou and Tsomokos (2008), Uthayakumar and Vaid (1998), and Sivathayalan and Vaid (2002) used the hollow cylinder apparatus to evaluate the influence of principal stress direction and intermediate principal stress on the onset of flow liquefaction. These studies consistently showed that sand specimens that were loaded under

a large intermediate principal stress or under large rotation of principal stress axis had a lower instability stress ratio. Experimental studies have also highlighted the role of initial fabric on instability triggering. For instance, Miura and Toki (1982); Tatsuoka et al. (1986); Vaid et al. (1999); Yang et al. (2008) and Sze and Yang (2014) showed that specimens prepared following different reconstitution methods while maintaining similar loading conditions exhibited significantly different behaviors, highlighting the initial fabric effects.

The instability onset associated with flow liquefaction has also been studied numerically and analytically with more efforts focusing on triaxial conditions. For example, based on experimental tests and numerical modeling, Been and Jefferies (2004) hypothesized that flow liquefaction could be triggered by a change in hardening modulus, rather than frictional properties. Lade (1992) used the Hill's instability criterion (Hill, 1958) to define an instability line for flow liquefaction. Borja (2006) used the bifurcation theory to establish a condition for liquefaction instability.

Andrade (2009) expanded the work of Borja (2006) by using a variation of the Norsand model (Jefferies, 1993) to evaluate the onset of instabilities under triaxial conditions and successfully predicted experimental data. Andrade et al. (2013) provided a closed-formulation of the instability criteria in terms of hardening modulus and stress ratio for the model of Dafalias and Manzari (2004). Mohammadnejad and Andrade (2015) generalized the instability criterion of Andrade et al. (2013) from triaxial conditions to general loading conditions and applied it to triaxial tests on Toyoura sand using the model by Dafalias and Manzari (2004). Buscarnera and Whittle (2012) and Lashkari (2016) used the difference between current and critical values of the plastic hardening modulus as an index for predicting the stress ratio at the onset of static liquefaction. Najma and Latifi (2017) used undrained stress paths and the instability definition at their peak to derive an instability criterion in terms of hardening modulus. A closed formulation was obtained for the model of Dafalias and Manzari (Dafalias and Manzari, 2004) and other constitutive models, focusing on triaxial conditions. This work was later expanded (Najma and Latifi, 2017, 2018) considering the multiaxial version of the model by Dafalias and Manzari (2004). These previous studies have emphasized that the predictive performance of the different instability criteria depends on

that of the constitutive model at play (Andrade, 2009; Andrade et al., 2013; Mohammadnejad and Andrade, 2015). Thus, including fabric anisotropy effects has not been feasible in these previous studies, due to the limitations of the constitutive models employed.

The studies by Lü et al. (2017) and Leguizamón-Barreto et al. (2021) are the only efforts that we are aware of exploring fabric and loading anisotropic effects on the onset of flow liquefaction. Lü et al. (2017) formulated a 3D cross-anisotropic model by incorporating a fabric tensor into the Mohr-Coulomb criterion. The second–order work criterion was used to identify the conditions for instability onsets. The formulation limited the study to cross-anisotropic sands. Leguizamón-Barreto et al. (2021) used the instability criteria derived by Mohammadnejad and Andrade (2015) combined with the model by Dafalias et al. (2004) to evaluate the onset of instability on hollow cylinder tests on Toyoura sand performed by Yoshimine et al. (1998). While this is a step forward, the model by Dafalias et al. (2004) does not account for fabric evolution and considers that the critical state line is evolving –an aspect that has later been found non-appropriate (Li and Dafalias, 2012; Theocharis et al., 2017; Wang et al., 2020) and inconsistent with the anisotropic critical state theory proposed by Li and Dafalias (2012).

In this study, we use the relatively new ACST framework formulated by Li and Dafalias (2012) to investigate the onset of instability in sands under undrained conditions considering the role of state, multiaxial loading and fabric anisotropy. To this end, we use the ACST-based SANISAND-F model developed by Petalas et al. (2020) to establish instability criteria in sands under undrained loading, for the most general form of fabric anisotropy features.

Our study is structured as follows. After a general introduction (Section 1), we briefly introduce the SANISAND-F model (Section 2). We then derive the fabric dependent undrained flow liquefaction instability criteria (Section 3) and describe the instability surface in the π-plane (Section 4). Next, we describe the evolution of soil state before and after instability during undrained multi-axial compression stress paths (Section 5). Then we propose a closed-form analytical equation to compute the stress ratio at instability and discuss its performance to reproduce numerical simulation results and experimental data (Section 6). Afterwards, we study the effect of the initial anisotropic consolidation on the onset of in-

stability (Section 7). We close the study with a discussion section (section 8) and the conclusions (section 9).

2. The SANISAND-F model

2.1. Model formulation

The SANISAND-F model was recently proposed in Petalas et al. (2020). It is an extension of the critical two-surface plasticity model presented in Manzari and Dafalias (1997) and Dafalias and Manzari (2004). The model is formulated within the ACST (Li and Dafalias, 2012), that accounts for the effect of fabric anisotropy on the mechanical behavior of granular soils. For a detailed presentation of the model and the ACST, the reader is referred to Li and Dafalias (2012) and Petalas et al. (2020).

The equations of the SANISAND-F model are summarized in Tables 1 and 2. In addition to the features of the DM04 (Dafalias and Manzari, 2004) model, the SANISAND-F model utilizes a deviatoric fabric tensor $\boldsymbol{F}$ (Eq. 1) as an evolving state variable. A scalar-valued Fabric Anisotropy Variable (FAV) A is then introduced as a measure of relative orientation between loading and fabric directions (Eq. 2). The original critical state conditions are enhanced as proposed in Li and Dafalias (2012) via Eq. 3, which denotes that at critical state the fabric and loading direction coincide. The isotropic state parameter ψ (Been and Jefferies, 1985) is enhanced with the effect of fabric via the dilatancy state parameter ζ in Eq. 4. The new state parameter determines the estimated dilatancy, which depends on fabric anisotropy, and the model's response becomes more contractive as the difference in fabric and loading orientation increases. Figure 2 geometrically summarizes the SANISAND-F constitutive model highlighting the constitutive surfaces and vector directions in the π-plane of the deviatoric stress-ratio space.

One of the limitations of the SANISAND-F model compared to other ACST based models in the literature (e.g. Gao et al. (2014)) is that due to the fact that fabric anisotropy mainly affects the dilatancy and the plastic modulus, and not the deviatoric plastic strain rate direction, the model leads to coaxiality between the stress and plastic strain rate tensors

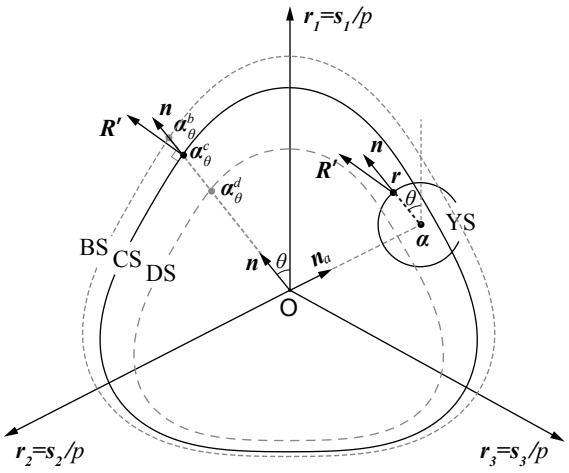

Figure 2: Illustration of the yield surface (YS), bounding surface (BS), dilatancy surface (DS) and critical surface (CS) on the deviatoric stress ratio space (from Petalas et al. (2020))

in radial loading (e.g. triaxial compression in an isotropically consolidated sample). The non-coaxiality between those two tensors was proven to have a significant effect when strain localisation initiation and evolution is simulated (see Gao and Zhao (2013)) in drained loading of dilative sands. However, in this study we focus on simulating the liquefaction triggering, assuming diffused instability without strain localization, and thus we expect that the effect of fabric in dilatancy dominates the effect of fabric via the non-coaxiality of stress and plastic strain rate tensors.

2.2. SANISAND-F vs DM04

The SANISAND-F model that is formulated within the ACST is an extension of the two-surface plasticity model (DM04) (Dafalias and Manzari, 2004) that is formulated within the classical critical state theory. The goal of this extension was to include the effect of fabric anisotropy, and thus, this effect is investigated in this section through simulations that assess the onset of flow instabilities. Isotropically consolidated, triaxial compression and extension laboratory tests conducted on Toyoura sand by Yoshimine et al. (1998) are simulated and illustrative results from the comparison are presented in Figure 3 to highlight the role of fabric.

Description	Equation	
Fabric tensor $\boldsymbol{F}$	$\boldsymbol{F} = F\boldsymbol{n}_F; \quad F = \sqrt{\boldsymbol{F} : \boldsymbol{F}}; \quad \boldsymbol{n}_F : \boldsymbol{n}_F = 1; \quad tr\boldsymbol{n}_F = 0$	(1)
FAV A	$A = \boldsymbol{F} : \boldsymbol{n}' = F\boldsymbol{n}_F : \boldsymbol{n}' = FN$	(2)
ACST conditions	$\eta = \eta_c = (q/p)_c = M(\theta); \quad e = e_c = \hat{e}_c(p); \quad A = A_c = 1$	(3)
DSP ζ	$\zeta = \psi - e_A(A-1)$	(4)
Elastic moduli	$G = G_0 p_{at} \frac{(2.97-e)^2}{1+e} \left(\frac{p}{p_{at}}\right)^{1/2}; \quad K = \frac{2(1+\nu)}{3(1-2\nu)} G$	(5)
Yield Surface	$f = [(\boldsymbol{s} - p\boldsymbol{\alpha}) : (\boldsymbol{s} - p\boldsymbol{\alpha})]^{1/2} - \sqrt{\frac{2}{3}} m\, p$	(6)
Flow rule	$\boldsymbol{R}^{'} = B\boldsymbol{n} - C\left(\boldsymbol{n}^2 - \frac{1}{3}\boldsymbol{I}\right)$	(7)
	$B = 1 + \frac{3}{2}\frac{1-c}{c} g(\theta) cos3\theta; \quad C = 3\sqrt{\frac{3}{2}}\frac{1-c}{c} g(\theta)$	(8)
Dilatancy surface	$\boldsymbol{\alpha}_\theta^d = \sqrt{\frac{2}{3}} \left[g(\theta) M_c exp(n^d \zeta) - m\right] \boldsymbol{n}$	(9)
Bounding surface	$\boldsymbol{\alpha}_\theta^b = \sqrt{\frac{2}{3}} \left[g(\theta) M_c exp(n^b < -\zeta >) - m\right] \boldsymbol{n}$	(10)
Critical state surface	$\boldsymbol{\alpha}_\theta^c = \sqrt{\frac{2}{3}} \left[g(\theta) M_c - m\right] \boldsymbol{n}$	(11)
Loading direction	$\boldsymbol{n} = \frac{\boldsymbol{r} - \boldsymbol{\alpha}}{\sqrt{2/3} m}$	(12)

Table 1: Main equations of the SANISAND-F model.

Description	Equation	
Dilatancy	$D = A_0 \left(\boldsymbol{\alpha}_\theta^d - \boldsymbol{\alpha}\right) : \boldsymbol{n} = \sqrt{2/3} A_d \left(M_\theta^d(\zeta) - \beta\right)$	(13)
Plastic Modulus	$K_p = pH(\boldsymbol{\alpha}_\theta^b - \boldsymbol{\alpha}) : \boldsymbol{n} = pH \left(M_\theta^b(\zeta) - \beta\right)$	(14)
	$H = \frac{2}{3} \frac{h(e,p,A)}{\langle (\boldsymbol{\alpha} - \boldsymbol{\alpha}_{in}) : \boldsymbol{n} \rangle} = \frac{2}{3} \frac{h(e,p,A)}{\langle \beta - \beta_{in} \rangle}$	(15)
	$h = G_0 h_1 exp(h_2 A)(e^{-1} - c_h)^2 \left(\frac{p}{p_{at}}\right)^{-1/2}$	(16)
Fabric evolution	$\dot{\boldsymbol{F}} = \langle L \rangle c_0 exp(A)(\boldsymbol{n}^{'} - r\boldsymbol{F})$	(17)
Strain increment	$\dot{\boldsymbol{\epsilon}} = \dot{\boldsymbol{\epsilon}}^e + \dot{\boldsymbol{\epsilon}}^p = \frac{1}{2G}\dot{\boldsymbol{s}} + \frac{1}{3K}\dot{p}\boldsymbol{I} + \langle L \rangle \left(\boldsymbol{R}^{'} + \frac{1}{3} D \boldsymbol{I}\right)$	(18)
Stress increment	$\dot{\boldsymbol{\sigma}} = 2G\dot{\boldsymbol{e}} + K\dot{\epsilon}_v \boldsymbol{I} - \langle L \rangle (3G\boldsymbol{R}^{'} + KD\boldsymbol{I})$	(19)
Plastic multipler	$L = \frac{1}{K_p} p\boldsymbol{n} : d\boldsymbol{r} = \frac{2G\boldsymbol{n} : \dot{\boldsymbol{e}} - K(\boldsymbol{n} : \boldsymbol{r})\dot{\epsilon_v}}{K_p + 2G - KD(\boldsymbol{n} : \boldsymbol{r})}$	(20)

Table 2: Main equations of the SANISAND-F model (continued).

The parameters for the DM04 model were calibrated by Dafalias and Manzari (2004) using triaxial compression tests performed by Verdugo and Ishihara (1996), but we observed that a re-calibration was required to match the experimental results from Yoshimine et al. (1998) better. To this end, we slightly adjusted some parameters, specifically: $c = 0.75$, $h_0 = 4.5$, $c_h = 1.0$, $n^b = 1.25$, $A_0 = 0.4$ and $n^d = 2.1$ (refer to Dafalias and Manzari (2004) for the rest of the parameters). For the SANISAND-F model, we used the parameters suggested by Petalas et al. (2020) (see Table 3) who calibrated the model against the experimental results from Yoshimine et al. (1998). In this study, the initial fabric tensor is characterized by transverse isotropy (cross-anisotropy) for the simulations (see $\boldsymbol{n}_F$ in Table 3), but note that ACST framework is amenable to generalized fabric tensors.

We simulated eight isotropically consolidated undrained triaxial compression and extension tests on samples with initial (after consolidation) relative density in the range $D_r = 22 - 30\%$ (Figure 3). The initial (after consolidation) mean effective stress was p_0= 50, 100, 300 and 500 kPa. Based on the simulation results, it can be observed that the DM04 model can accurately reproduce the triaxial compression tests with a single set of material parameters, while it fails to predict the onset of static liquefaction as well as the significantly lower undrained shear strength in the triaxial extension experiments. In contrast, simulation results with the SANISAND-F model match both the triaxial compression and extension test results. In all cases, the initial fabric can be assumed similar (as similar reconstitution procedures were used), but the loading direction is different in triaxial compression and extension; hence, the results in Figure 3 highlight the coupling between fabric and loading direction (i.e., fabric anisotropy) on the overall response, which can be captured under the ACST framework and the SANISAND-F model, but not with the DM04 model.

3. Flow liquefaction instability criteria

In this section we derive analytical flow instability criteria using the fabric-dependent multiaxial SANISAND-F constitutive model for undrained loading, following the procedure presented in Najma and Latifi (2017).

Table 3: Material parameters of the SANISAND-F model, calibrated for Toyoura Sand (from Petalas et al. (2020))

Description	Symbol	Values
Elasticity	G_0	125
	v	0.05
Critical state	e_{ref}	0.934
	ξ	0.7
	λ	0.019
	M_c	1.25
	c	0.75
Plastic modulus	h_1	7.5
	c_h	0.85
	n^b	1.4
Yield surface	m	0.01
Dilatancy	A_0	0.704
	n^d	3.5
Fabric	e_A	0.0818
	F_{in}	0.5
	c_0	5.2
	h_2	1.3
	$\boldsymbol{n}_F$	$\begin{bmatrix} \frac{2}{\sqrt{6}} & 0 & 0 \\ 0 & \frac{-1}{\sqrt{6}} & 0 \\ 0 & 0 & \frac{-1}{\sqrt{6}} \end{bmatrix}$

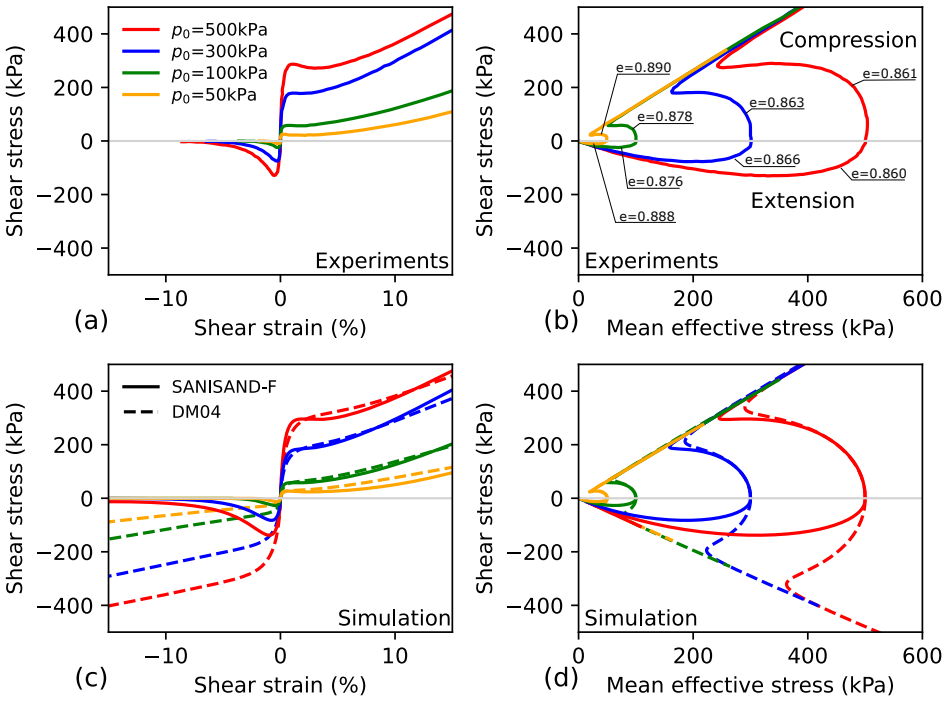

Figure 3: Performance of DM04 and SANISAND-F constitutive models for triaxial compression and extension tests from Yoshimine et al. (1998)

3.1. Instability Criterion 1: Plastic Modulus

In undrained loading conditions, the rate of total volumetric strain is zero.

$$d\varepsilon_v = d\varepsilon_v^e + d\varepsilon_v^p = 0 \tag{21}$$

Considering the volumetric part of the total strain rate given in Eq. 18, Eq. 21 is written as:

$$d\varepsilon_v = \frac{dp}{K} + \langle L \rangle D = 0 \tag{22}$$

During elasto-plastic loading, the plastic multiplier L is positive and equal to $\frac{1}{K_p} p\boldsymbol{n} : d\boldsymbol{r}$, according to Eq. 20. Thus, Eq. 22 is rewritten as:

$$\frac{dp}{K} + \frac{D}{K_p} p\boldsymbol{n} : d\boldsymbol{r} = 0 \tag{23}$$

Thus, the plastic modulus that satisfies the zero volumetric strain constraint is given by:

$$K_p = -KDp\boldsymbol{n} : \frac{d\boldsymbol{r}}{dp} \tag{24}$$

The deviatoric stress ratio is defined as $\boldsymbol{r} = \frac{\boldsymbol{s}}{p}$, which implies $\frac{d\boldsymbol{r}}{dp} = \frac{1}{p}(\frac{d\boldsymbol{s}}{dp} - \frac{\boldsymbol{s}}{p})$. During the onset of undrained flow instability, $\frac{d\boldsymbol{s}}{dp} = 0$ (Najma and Latifi, 2017, 2018), which implies $\frac{d\boldsymbol{r}}{dp} = \frac{-\boldsymbol{r}}{p}$. This simplifies Eq. 24 as:

$$K_{p,f} = KD\,\boldsymbol{n} : \boldsymbol{r} \tag{25}$$

where $K_{p,f}$ is the plastic modulus at the onset of the flow liquefaction. Then, we write the first instability criterion as $H_1 = 0$, where

$$H_1 = K_p - K_{p,f} \tag{26}$$

and K_p is the current bulk modulus. We show later that H_1 becomes zero for a second time after the onset of undrained flow instability, if the material exhibits a change from contractive to dilative behavior.

The general form of Eqs. 25 and 26 is the same as those proposed in the isotropic flow instability criterion of Najma and Latifi (2017). However, since $K_{p,f}$ is a function of dilatancy D, and in this work D is a function of the anisotropic dilatancy state parameter ζ (see Eq. 13), the derived instability criterion of Eq. 26 is also fabric-dependent.

3.2. Instability Criterion 2: Stress Ratio

The three constitutive ingredients in Eq. 25 are the elastic bulk modulus K, the dilatancy D and the plastic modulus K_p, which are defined based on the SANISAND-F model in Eqs. 5, 13 and 14 respectively. Substituting them in Eq. 25 and denoting β as β_f, the stress ratio at the onset of flow liquefaction, we get:

$$\frac{(M_\theta^b - \beta_f)}{\beta_f(\beta_f - \beta_{in})(M_\theta^d - \beta_f)} = \underbrace{\frac{2A_d(1+\nu)(2.97-e)^2}{3(1-2\nu)(1+e)h_1 exp(h_2 A)(e^{-1}-c_h)^2}}_{F_e} \tag{27}$$

After rearranging:

$$\beta_f^3 - (\beta_{in} + M_\theta^d)\beta_f^2 - \left(\frac{1}{F_e} - \beta_{in}M_\theta^d\right)\beta_f + \frac{M_\theta^b}{F_e} = 0 \tag{28}$$

Eq. 28 can be recast in a simple cubic polynomial form as shown below:

$$\beta_f^3 + C_1\beta_f^2 + C_2\beta_f + C_3 = 0 \tag{29}$$

with $C_1 = -\left(\beta_{in} + M_\theta^d(\zeta)\right)$, $C_2 = -\left(\frac{1}{F_e} - \beta_{in}M_\theta^d(\zeta)\right)$, and $C_3 = \frac{M_\theta^b(\zeta)}{F_e}$. As shown in Najma and Latifi (2017), the general cubic polynomial has three roots, of which two are imaginary and one is a real acceptable root. The real root can be estimated as (Najma and Latifi, 2017):

$$\begin{aligned} \beta_f = \frac{-C_1}{3}\left[1 + 2\left(1 - 3\frac{C_2}{C_1^2}\right)^{0.5} cos\left(\frac{\phi + 4\pi}{3}\right)\right] \\ \phi = cos^{-1}\frac{1 + \frac{27C_3}{2C_1^3} - \frac{9C_2}{2C_1^2}}{\left(1 - \frac{3C_2}{C_1^2}\right)} \end{aligned} \tag{30}$$

At the initiation of flow liquefaction, the stress ratio β is equal to β_f. We rewrite this second instability criterion as $H_2 = 0$, where:

$$H_2 = \beta - \beta_f \tag{31}$$

Again, the general form of Eqs. 30 and 31 is consistent with that proposed in Najma and Latifi (2017); however, the terms C_1, C_2, C_3 and F_e depend on fabric anisotropy in this

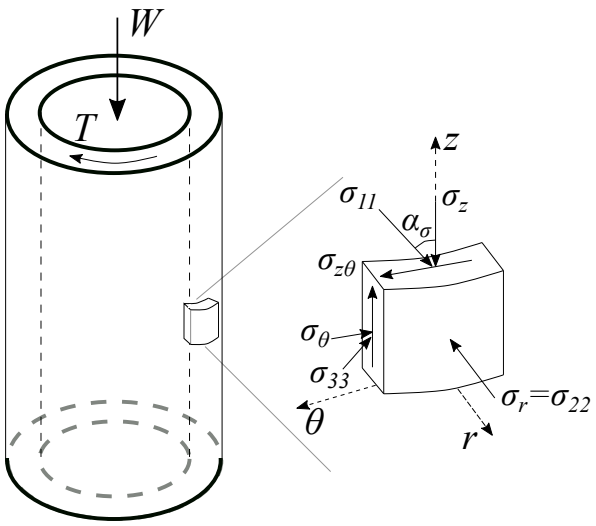

Figure 4: Element in a hollow cylinder specimen showing stress components

study, via the DSP ζ and FAV A. This dependence is the critical component that allows us to introduce the effects of fabric anisotropy on the onset of flow liquefaction.

4. Numerical prediction of the flow instability

In this section we use the SANISAND-F model to predict flow instability based on the criteria discussed in the previous section. Here, we simulate hollow cylinder shear tests as this type of test allows investigating fabric anisotropy and intermediate stresses. In addition, we will use the previously discussed SANISAND-F parameters calibrated for Toyoura sand (Table 3).

Figure 4 shows the typical configuration of a hollow cylinder test where the normal stresses σ_z, σ_θ, σ_r and the shear stress $\sigma_{z\theta}$ can be independently controlled. The angle $\alpha_\sigma = \frac{1}{2} tan^{-1} \frac{2\sigma_{z\theta}}{\sigma_\theta - \sigma_z}$ is referred to as the angle between the principal stress σ_{11} and the vertical z-axis. If the principal stresses are in the order $\sigma_{11} > \sigma_{22} > \sigma_{33}$, the intermediate stress ratio is given by $b = (\sigma_{22} - \sigma_{33})/(\sigma_{11} - \sigma_{33})$, which is also related to the Lode angle, $\theta = \frac{\pi}{6} + tan^{-1}\left(\frac{2b-1}{\sqrt{3}}\right)$.

Figures 5a and 5b show the evolution of the instability criteria H_1 and H_2 while Figures 5c and 5d show the stress-strain response of numerical simulations performed at an initial

void ratio of 0.89, and confining stress of $p_0 = 500$kPa for the loading path with constant $\alpha_\sigma = 45^o$, and $\theta = 30^o$.

It can be observed that the first criterion yields two instances where $H_1 = 0$ (see Fig. 5a): the first point marks the onset of flow liquefaction, while the second represents a change from contractive to dilative behavior, also known as the transformation point (Andrade, 2009; Andrade et al., 2013; Ishihara, 1996). By contrast, the $H_2 = 0$ criterion (see Fig. 5b) predicts only the onset of flow liquefaction point. It is important to note that both H_1 and H_2 criteria are consistent in identifying the onset of flow liquefaction, and from here on, unless specified, we use only the H_2 criterion to predict flow liquefaction instability.

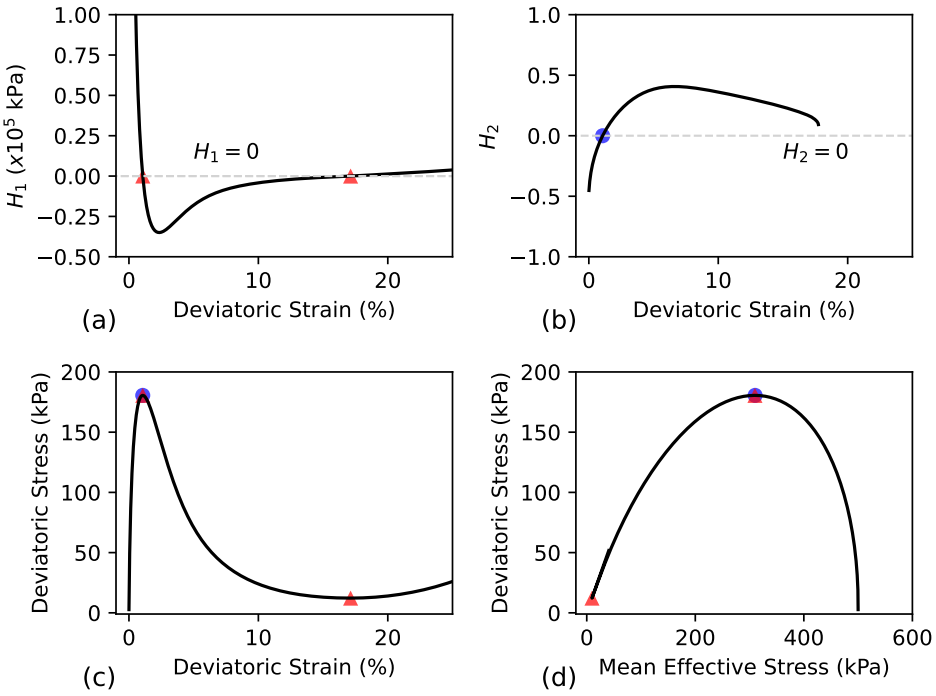

Figure 5: SANISAND-F simulations of a hollow cylinder test for $\alpha_\sigma = 45^o$ and $b = 0.5$ on Toyoura sand with e=0.89 and p_0=500 kPa, showing (a) the H_1 criterion; (b) the H_2 criterion; (c) the stress-strain response, and (d) the stress path.

Next, to illustrate the concept of an instability surface, we conduct simulations at constant $\alpha_\sigma = [0^o, 45^o]$ and varying the Lode angle, θ, with values from 0^o to 360^o. The instability points predicted from these simulations can be plotted in a π-plane of the de-

viatoric stress-ratio space to visualize an instability surface, as shown in Figure 6. Note that the Lode angle $\theta = 0^o$ corresponds to $b = 0$ while $\theta = 60^o$ corresponds to $b = 1$. For $\theta > 60^o$ only the Lode angle will be used to refer the loading path. The instability surface separates the stable stress states from the unstable stress states in terms of flow liquefaction. Interestingly, it can be observed that the instability surface is not symmetrical with respect to all the major axes in the stress space (i.e., the $\theta = 0^o$-$\theta = 180^o$, $\theta = 60^o$-$\theta = 240^o$, and $\theta = 120^o$-$\theta = 300^o$ axes), as typically observed in constitutive models under the classical critical state framework (e.g., DM04). This is attributed to the effect of fabric anisotropy that is incorporated by the ACST framework. Note that when $\alpha_\sigma = 0^o$ the instability surface is symmetrical with respect to the major axes, $\theta = 0^o$-$\theta = 180^o$ in stress space (refer Figure 6a). This is due to the fact that when $\alpha_\sigma = 0^o$ the principal axes of loading and fabric tensor align with each other thus allowing symmetry in the horizontal directions.

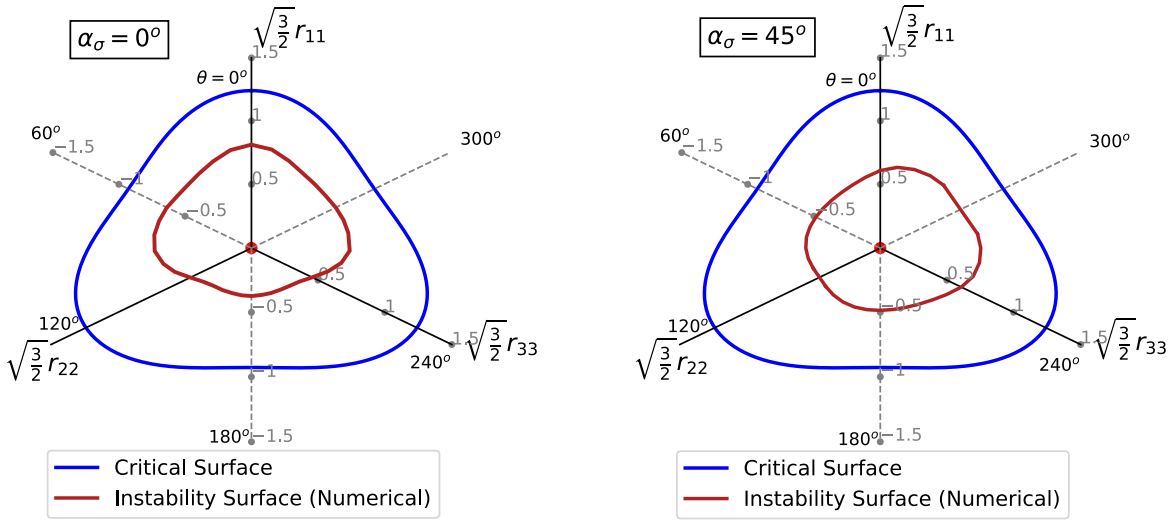

(a) (b)

Figure 6: Instability surface obtained from the numerical simulations of a hollow cylinder test with constant Lode angle (θ) and constant stress principal axis rotation (α_σ) using Toyoura sand properties with e=0.89 and p_0=500 kPa (a) for $\alpha_\sigma = 0^o$ (b) for $\alpha_\sigma = 45^o$

5. Stress principal axis rotation, Lode angle, and fabric effects on the onset of flow liquefaction

A series of numerical simulations with varying stress principal axis rotations (α_σ), Lode angle (θ) and initial fabric intensity (F_{in}) are performed in this section, to investigate their effect on the triggering of flow instability. Note here that stress principal axis rotation represents constant and fixed rotation of α_σ during undrained shearing. Moreover, undrained hollow cylinder experiments performed by Yoshimine et al. (1998) on Toyoura sand are simulated for validation of the modelling procedure. All the simulations are done with SANISAND-F and the set of parameters presented in Table 3.

5.1. Effect of stress principal axis rotation α_σ

Figure 7 presents the simulation results of tests with initial void ratios in the range of 0.821-0.828, initial confinement $p'_0 = 100$ kPa, $\theta = 30^o$ ($b = 0.5$), and different α_σ values i.e., $[15^o, 30^o, 45^o, 60^o, 75^o]$. The experimental results from Yoshimine et al. (1998) are also presented for comparison. In the experiments, the instability point (marked with an open circle) corresponds to the local peak in the $p' - q$ space. The instability criterion of Eq. 30 is also tracked for the numerical simulations and the open circles on the numerical-based curves correspond to the stress ratios satisfying it.

The increasing contractive behavior with the increase of α_σ is well captured by the SANISAND-F model, which also reproduces with acceptable accuracy the stress-strain response as also discussed in Petalas et al. (2020). In all cases, corresponding to experiments, after the flow instability point, a phase transformation from a contractive to dilative tendency is observed. This response is also well captured with the model.

Figure 8 shows the instability surfaces on the deviatoric plane estimated for loading paths with different α_σ, using the procedure discussed in Section 4. Note that the instability surface is discontinuous due to the fact that flow instability does not occur for every combination of angles θ and α_σ. For example, the surface is not defined for $\theta = 30^o$ when $\alpha_\sigma = 15^o, 30^o$, and 45^o (i.e., there is no instability onset), but it is defined for $\alpha_\sigma = 60^o$ and 75^o, which is consistent with the results in Figure 7. Of note, instability may be still triggered for other θ

values (i.e., other loading paths) where the instability surface is defined when $\alpha_\sigma = 15^o, 30^o$, and 45^o as illustrated in Figure 8. Interestingly, for a loading path in the downward r_{11} direction (i.e., $\theta = 180^o$), we can see that there is an instability onset for $\alpha_\sigma = 15^o$, but not for $\alpha_\sigma = 75^o$, which is apparently in contrast with the observations in Figure 7. However, this observation is associated with the coupled effects between the loading direction and fabric orientation. The quantity N (refer to Table 1) measures the relative orientation between the fabric and loading directions. If the fabric and loading have the same direction (i.e., $N = 1$), the computed behavior shows a hardening response. As the difference between the fabric and loading directions increases a softening response is enhanced. These observations are consistent with the results in Figure 7 where as α_σ decreases N increases (i.e., it gets close to 1), causing an enhanced hardening response. For the $\theta = 180^o$ loading path, when $\alpha_\sigma = 15^o$ the initial value of N is -0.89 causing a softening response that triggered an instability condition. Whereas when $\alpha_\sigma = 75^o$ the initial value of N is 0.41, causing a hardening behavior with no instability triggering.

5.2. Effect of lode angle θ (or intermediate stress ratio b)

Figure 9 shows the SANISAND-F simulations of undrained tests on Toyoura sand with void ratio $e = 0.855$, initial confinement $p'_0 = 100$ kPa, α_σ equal to 45^o, and different θ values, i.e., $[0^o, 13.9^o, 30^o, 46.1^o, 60^o]$ (corresponding to $b = [0, 0.25, 0.5, 0.75, 1]$) using the same set of parameters as in previous simulations (i.e., Table 3). The experimental results from Yoshimine et al. (1998) are also presented for reference. Note the void ratio in experiments varies from $e = 0.849 - 0.861$. A representative mid-value for the void ratio of $e = 0.855$ is selected for simulations. The numerical results are qualitatively consistent with the experimental results, i.e., as the b value increases, a more contractive response with lower peak values is observed. Notice also that there are more differences in the dilatancy response (i.e., experimental versus numerical) at large strains for large b values, which may be attributed to the dilatancy scaling in SANISAND-F. However in assessing instability conditions the post-peak response is, comparatively, not as important as assessing the triggering (Sadrekarimi, 2014). The instability points estimated by the criterion H_2 are also presented in Figure 9.

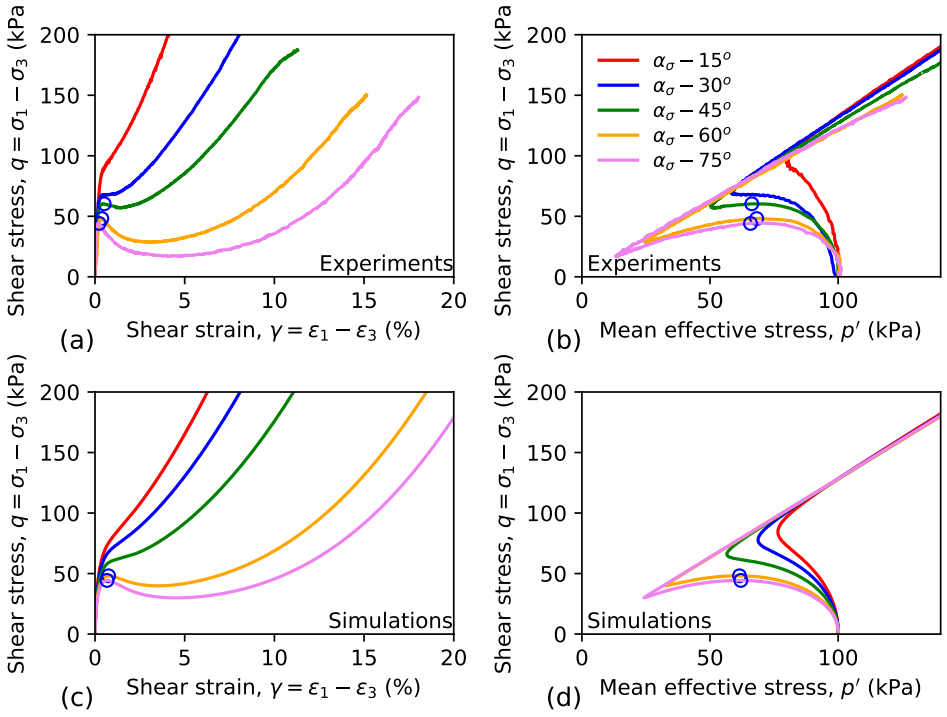

Figure 7: Experimental data (a,b) and SANISAND-F simulations (c,d) for undrained shearing with constant $\theta = 30^o$ ($b = 0.5$) and constant α_σ=$15^o - 75^o$ on Toyoura sand with e=0.821-0.828. Data after Yoshimine et al. (1998). The instability points in both experiments and simulations (from the H_2 criterion) are represented by a blue circular marker.

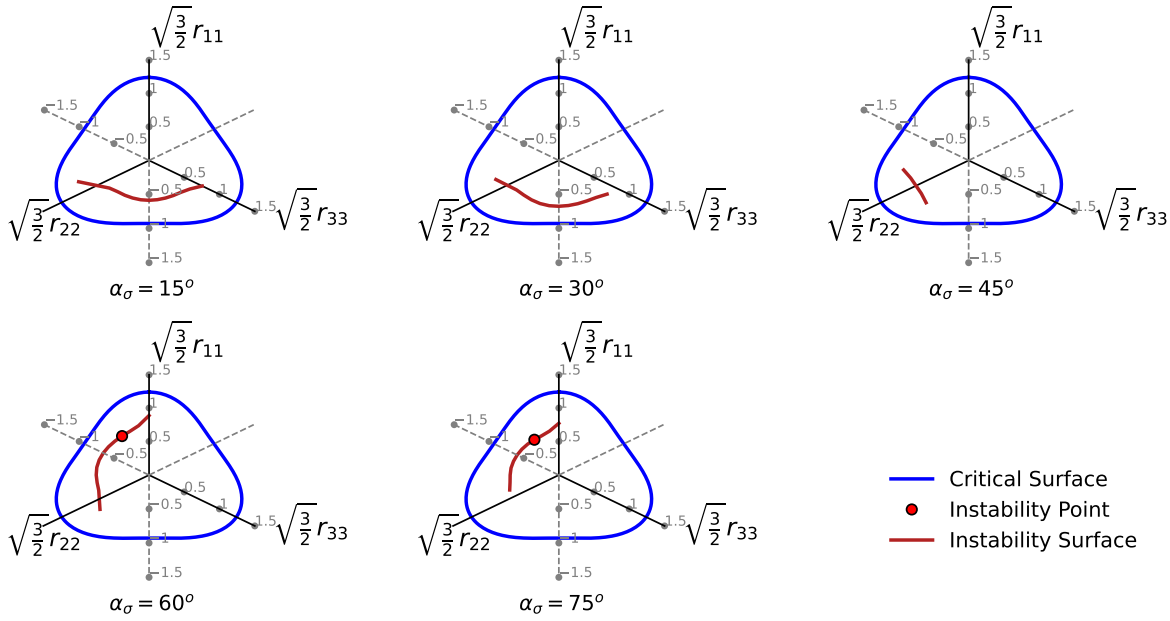

Figure 8: Numerical estimation of instability surfaces for tests with constant $\alpha_\sigma = [15^o - 75^o]$ on Toyoura sand with e=0.821-0.828. Instability points corresponding to $b = 0.5$ ($\theta = 30^o$) are plotted on instability surfaces when defined (for $\alpha_\sigma = 60^o$ and $\alpha_\sigma = 75^o$).

The estimated instability surface for $\alpha_\sigma - 45^o$ is presented in Figure 10, which also shows the instability points for different b values. In Figure 9, instability triggers for all the considered b values, which is consistent with Figure 10. In addition, the instability stress ratios (i.e., the distance from the instability surface to the origin) decrease as b increases, which is in agreement with the previous discussions. For higher Lode angles, i.e., θ from 250^o to 350^o, the simulations show hardening responses, and thus the instability surface is not defined.

5.3. Initial soil fabric effects

To assess the effect of the initial fabric on the instability surface. A sensitivity analysis is performed using different fabric intensities for the initial cross-anisotropic fabric direction. Figures 11 (a) and (b) show the undrained constitutive response obtained for a constant loading path with $\alpha_\sigma = 0^o$ and $\theta = 0^o$ (triaxial compression loading), a void ratio $e = 0.89$, an initial confinement pressure $p'_0 = 500$ kPa, and a variable initial fabric intensity $F_{in} = [0.01, 0.5, 1.0]$, which includes the typical range of $F_{in} = 0 - 0.6$ for Toyoura sand in different

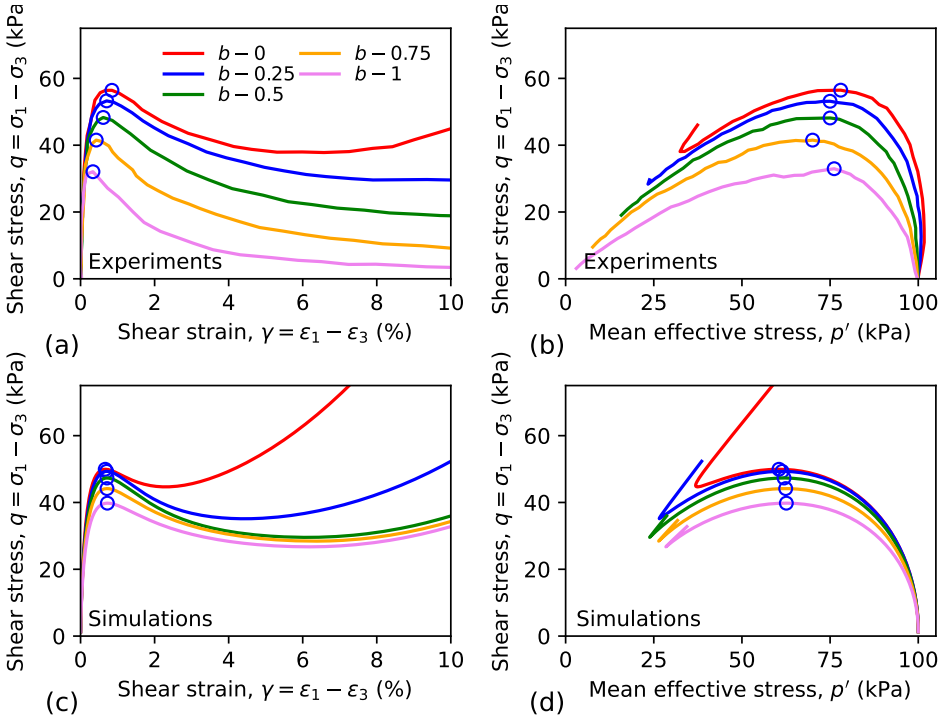

Figure 9: Experimental data (a,b) and SANISAND-F simulations (c,d) for undrained shearing with constant $\alpha_\sigma = 45^o$ and constant b=0 to 1 (or $\theta = 0^o$ to 60^o) on Toyoura sand with e=0.855. Data after Yoshimine et al. (1998). The instability points in both experiments and simulations (from the H_2 criterion) are represented by blue circular markers.

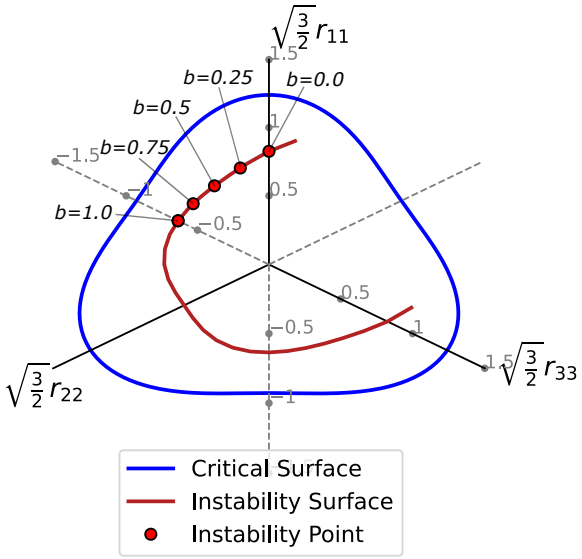

Figure 10: Numerical estimation of the instability surface for a stress path with constant $\alpha_\sigma = 45^o$ on Toyoura sand with e=0.855 and $p'_{in} = 100$ kPa. Instability points corresponding to $b = 0$ to 1 (or $\theta = 0^o$ to 60^o) are plotted on the instability surface.

sample preparation methods (Gao and Zhao, 2015). Note that $F_{in} = 0.01$ represents a nearly isotropic fabric and $F_{in} = 1.0$ represents a highly anisotropic fabric. Such extreme fabric intensities are chosen along with the value $F_{in} = 0.5$ (recommended in Petalas et al. (2020)) to highlight the influence of initial fabric on a wide range. It is observed that the constitutive behavior becomes more dilative as the fabric intensities increase from 0.01 to 1.0 (see Fig. 11a,b). In fact, for a fabric intensity of $F_{in} = 1.0$, there is no instability point detected. This is because, in the ACST framework the fabric anisotropy variable, $A = FN$, controls the contractive (lower value of A) or dilative (higher value of A) behavior of the constitutive response in undrained loading. Where F is the fabric intensity and N is the relative orientation between fabric and loading directions. For the three cases in Figure 11(a,b), the value of $N = \boldsymbol{n}_F : \boldsymbol{n}'$ is equal to 1, this is because the cross-anisotropic fabric (triaxial compression like fabric direction) and the triaxial compression loading has the same orientation. Thus the value of A is equal to F and for higher initial fabric intensity

the constitutive response is more dilative and the instability stress-ratio is higher. Figures 11 (c) and (d) show results of numerical simulations conducted with constant $\alpha_\sigma = 0^o$ and $\theta = 180^o$. It is now observed that the fabric intensity has an inverse effect on the constitutive response and the instability stress-ratio compared to the triaxial compression loading path. This is because, for the new loading path the value $N = -1$, implying $A = -F$, and thus causing the inverse effect. This highlights that the overall observed response (e.g., the instability triggering) is intimately related to coupled effects between the initial fabric and the imposed loading paths, which is at the core of the ACST framework. This is further illustrated in Figure 12, which shows the effect of fabric intensity on the instability surface represented in the π-plane for loading paths with constant $\alpha_\sigma = 0^o$. The effect of initial fabric intensity is clearly evident from the shapes of the instability surfaces. For $\alpha_\sigma = 0^o$, the highest influence of fabric intensity on the instability point is observed for loading paths with θ values close to zero. The initial fabric effects at other loading paths such as $\theta = 60^o$, $\theta = 180^o$, $\theta = 300^o$ are also substantial.

6. Analytical prediction of instability surfaces and stress ratios

The instability stress ratio (β_f) derived in Equation 30 is a function of the SANISAND-F parameters, A, ζ, and loading conditions (i.e., θ, α_σ). Given fixed loading and initial conditions, A and ζ evolve to their values when flow instability occurs. However, this evolution does not significantly affect the estimation of β_f. This is illustrated in Figure 13 using SANISAND-F for a simulation on Toyoura sand with $e = 0.89$, $p_0 = 500$ kPa, $\alpha_\sigma = 45^o$, and $b = 0.5$. Figures 13 a and b show the stress-strain response and three snapshots of the stress path, namely: (i) the initial condition when the loading starts, (ii) the instability onset, and (iii) a condition near to the critical state. Figure 13c shows the evolution of the dilatancy state line (DSL). Interestingly, the DSL does not evolve significantly from configuration (i) to configuration (ii). A similar observation can be made for A, $M^d_\theta(\zeta)$, $M^b_\theta(\zeta)$, and ζ (Figures 13 d, e, and f),(i.e., there is no significant evolution from configuration (i) to configuration (ii)). The DEM study by Salimi and Lashkari (2020) also supports this observation where the authors showed that the fabric, defined as the particle orientation tensor, did not show

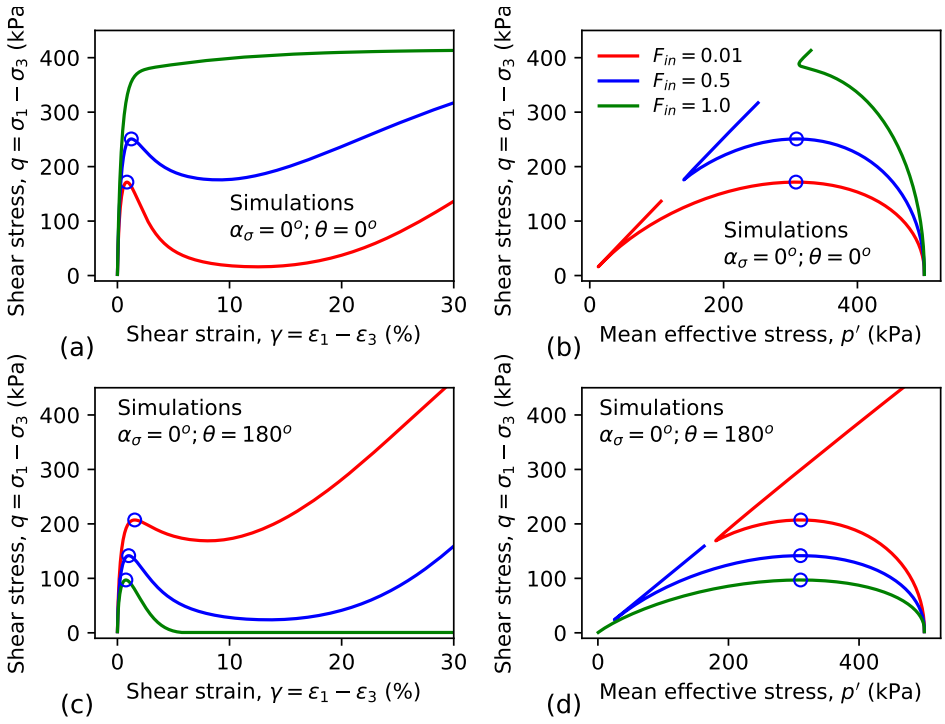

Figure 11: SANISAND-F simulations of undrained shearing with initial state of e=0.85, p'_{in} = 500kPa and different fabric intensities $F_{in} = [0.01, 0.5, 1.0]$ subjected to constant α_σ=0^o and $\theta = 0^o$ ($b = 0$) in (a) and constant α_σ=45^o and $\theta = 0^o$ ($b = 0$) in (b) . The instability points from the H_2 criterion are represented by blue circular markers.

significant evolution from the initial state to the instability state. This implies that the effect of fabric evolution is not significant until the onset of instability and thus the instability state could be approximated by assuming $A_f = A_{in}$ and $\zeta_f = \zeta_{in}$, where the subscripts f and in refer to the instability and initial conditions, respectively. This is practical as the instability stress ratio β_f could be estimated directly by using SANISAND-F parameters, A_{in}, and ζ_{in}, which act as inputs into the analytical instability equation (Eq. 30).

Under these considerations, the instability surface in the π-plane can also be estimated directly from Equation 30 using the following steps:

1. Calculate A, from the initial fabric tensor $\boldsymbol{F}_{in}$ and the unit-norm deviatoric stress-ratio tensor ($\boldsymbol{n}''$) or loading direction. For the desired Lode angle (θ) one can obtain $\boldsymbol{n}''$. Note that the tensor $\boldsymbol{F}_{in}$ should be represented in the principal stress axes. Thus, a

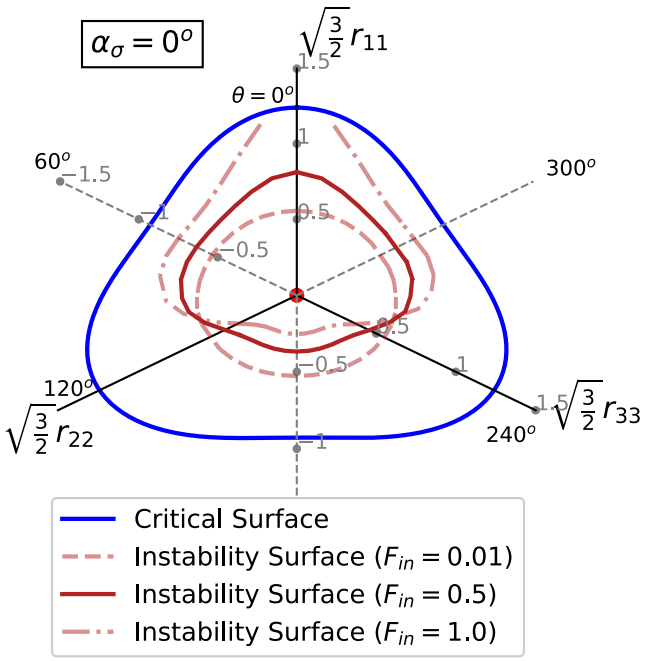

Figure 12: Effect of initial fabric intensity on the instability surface obtained for various loading paths, θ varying from 0^o to 360^o with constant $\alpha_\sigma = 0^o$

rotation of the fabric tensor from global stress axes (z, θ, r) to the principal stress axes (11, 22, 33) needs to be performed prior to the computation of A. The rotation matrix can be computed from the loading angle α_σ.

2. Calculate F_e for the given void ratio e, material parameters, and the initial A from Equation 27.
3. Calculate M_b^θ, M_c^θ and M_d^θ from material parameters and ζ for the desired Lode angle θ. ζ can be obtained from e, the initial p_0' and A.
4. Calculate instability stress ratio from Equation 30 using the factors presented in Equation 29.
5. Estimate the instability surface in the π-plane by iterating on different values of the Lode angle θ.

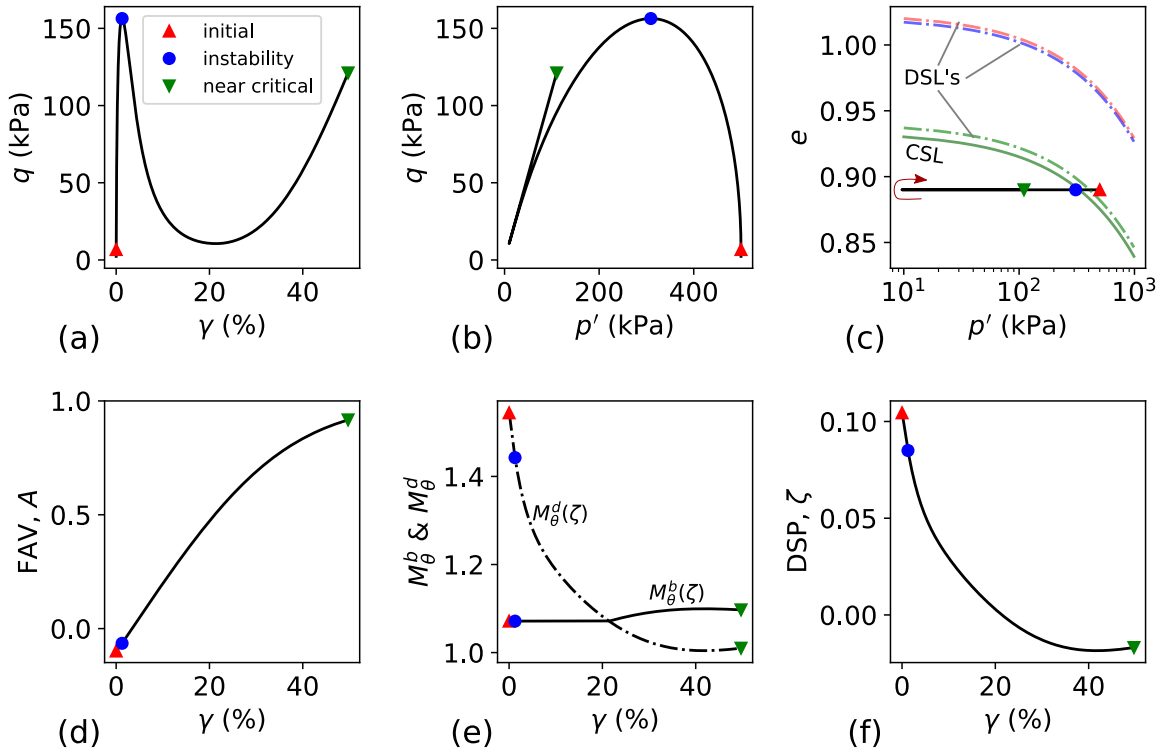

Figure 13: Evolution of Fabric Anisotropy Variable w.r.t the stress state. The FAV values at three stages of the undrained response are shown.

Using the steps listed above, Figure 14a shows the estimated instability surface for $\alpha_\sigma = 45^o$ in the π-plane. Figure 14a also highlights the numerical instability surface (i.e., considering the exact A and ζ values at instability) for comparison purposes. It can be observed that the analytically estimated instability surface approximates with acceptable accuracy the numerical solution. Another point to highlight is that the instability surface is not symmetrical with respect to the origin in the π-plane. This is due to the fact that within the ACST framework, the relative effects of soil fabric and the loading direction are taken into account in the estimation of the instability stress ratios. Thus, the resistance to flow liquefaction (represented as the distance between the origin and the instability surface) changes as a function of the Lode angle θ, and it is also influenced by fabric anisotropy. To further illustrate the application of the analytical estimation of instability surfaces, Figure 14b shows instability surfaces for Toyoura sand with $e = 0.89$, $p'_0 = 500$, α_σ values from 0^o

to 90^o, and θ varying from 0^o to 360^o.

Lastly, Figure 14c compares instability stress ratios estimated numerically and analytically, against the instability stress ratios from the experiments on Toyoura sand considered in this study (Yoshimine et al., 1998). When the computed instability stress ratio (η_f^{com}) matches the experimental instability stress ratio (η_f^{exp}), the data points lie on the $x = y$ line (highlighted in the plot). The results are presented for the cases that showed flow or limited flow behavior. As it can be observed, both the numerical and analytical predictions match experimental results relatively well. Importantly, all our simulations used the SANISAND-F model with a fixed set of parameters (i.e., Table 3), which were used under a variety of loading conditions (i.e., considering intermediate stresses and fabric anisotropy). The results highlight the usefulness of the ACST framework for estimating the instability onset under generalized undrained loading conditions.

7. Influence of initial consolidation on the onset of instability

Assessing the instability conditions imposed by an undrained loading on a material that has been anisotropically consolidated is of interest, for example, for anisotropic consolidated triaxial tests (also known as K_0 triaxial compression tests). When simulating an element test that involves anisotropic consolidation by the use of a constitutive driver (Bardet and Choucair, 1991), the method for initialization of the stress state and state variables after consolidation (before undrained shearing) affects the results. In this work, we consider two different methods, namely Method 1 and Method 2, for reference. In Method 1, the anisotropic stress state after consolidation is directly assigned as input to the algorithm and state variables (e.g., void ratio, etc.) are equal with the ones in the element test after the process of consolidation. In Method 2, the simulation is performed in two steps. First, the anisotropic consolidation is simulated, and then the undrained shearing is imposed.

In bounding surface plasticity models for sands, like DM04 or SANISAND-F, the above mentioned choices affect the simulated stiffness of the material during undrained shearing and thus the simulated flow instability stress ratio that is of interest in this work. More specifically, the simulation results are sensitive on the determination of $\boldsymbol{\alpha_{in}}$ tensor in the

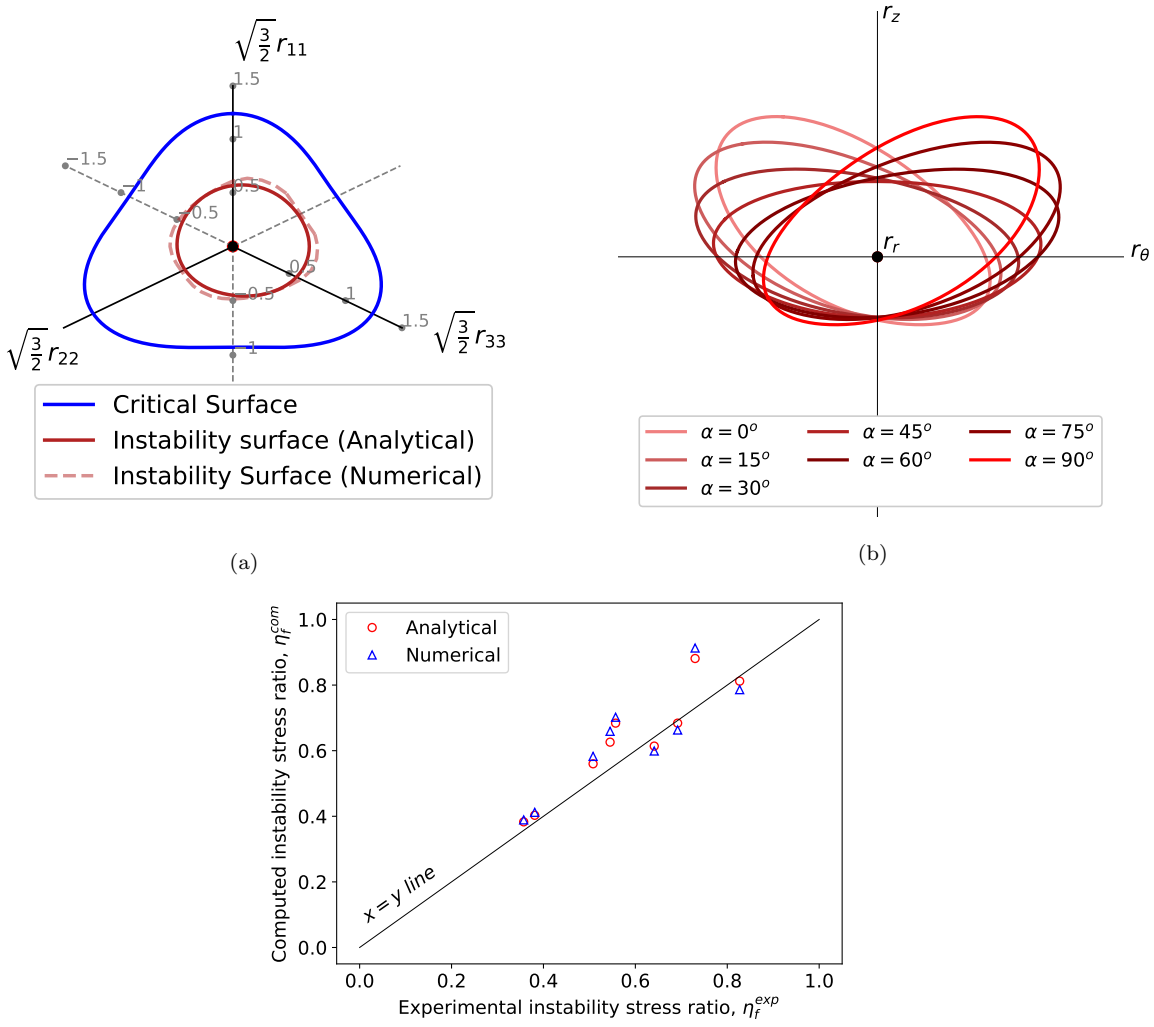

(a)

(b)

(c)

Figure 14: Analytical estimation of instability surface/ratio for loading paths with constant α_σ and b (a) Comparison of instability surface predicted from the proposed analytical equation and the instability points predicted from the numerical simulations (b) Estimation of instability surface for various α_σ in global deviatoric stress-ratio coordinate axes (c) Stress ratio at instability according to the analytical and numerical methods, plotted against the experimental data

denominator of Eq. 15. $\boldsymbol{\alpha_{in}}$ is the value of $\boldsymbol{\alpha}$ at the initiation of a new loading process (e.g. unloading after loading), which is signified by the zero or negative value of the quantity $(\boldsymbol{\alpha} - \boldsymbol{\alpha}_{in}) : \boldsymbol{n}$ within $\langle\rangle$ in the denominator. When $(\boldsymbol{\alpha} - \boldsymbol{\alpha}_{in}) : \boldsymbol{n} \leq 0$, i.e., a new loading process is determined, $K_p \approx \infty$; thus, the model predicts very small plastic strain increment (the step becomes elastic) and $\boldsymbol{\alpha}_{in}$ is updated to $\boldsymbol{\alpha}$. Therefore, after the initiation of a new loading process the behavior becomes elastic with very high stiffness for the first few steps, until K_p starts to decrease again due to elasto-plastic behavior.

We use the two methods (Method 1 and 2) to simulate undrained compression and extension shearing on Toyoura sand, on anisotropically consolidated samples, considering an initial void ratio of 0.915, $p_0^{'} = 100kPa$ and a consolidation ratio $K_c = \sigma_{hc}^{'}/\sigma_{vc}^{'} = 0.8$. $\sigma_{hc}^{'}$ and $\sigma_{vc}^{'}$ are the horizontal and vertical effective stresses before the undrained shearing. The discussion on the modeling strategy is relevant because, to our knowledge, previous numerical studies have explored the effects of anisotropic consolidation by using Method 1 (e.g., Najma and Latifi (2017)). Figure 15 shows the simulation results, highlighting the difference between the two methods. In Method 1 only the undrained shearing phase is simulated and the initial back-stress ratio $\boldsymbol{\alpha_{in}}$ is set to be equal with the stress ratio $\boldsymbol{r} = \boldsymbol{\alpha}$ at the end of consolidation. On the other hand, in Method 2, $\boldsymbol{\alpha_{in}} = \boldsymbol{0}$, due to the fact that the consolidation process is simulated starting from a zero stress and back-stress state, and there is no new loading process initiated (i.e., there is no reversal of loading direction) from the beginning until the end of the phase that updates $\boldsymbol{\alpha_{in}}$.

In Method 1, $(\boldsymbol{\alpha} - \boldsymbol{\alpha}_{in}) : \boldsymbol{n} = 0$ during the initiation of both undrained compression and extension, which makes the denominator of the plastic modulus in Eq. 15 infinity, and thus, the plastic part of the total strain negligible. Practically, during undrained shearing, the stiffness initially is elastic, and that it is observed in Figure 15b, where the stress path initiates with a vertical orientation (no decrease in mean effective stress) for both cases. This leads to a larger peak deviatoric stress in triaxial compression compared to Method 2 (Figure 15b and d). This is due to the fact that in Method 2, during the consolidation simulation $\boldsymbol{\alpha}_{in}$ remains zero (no loading reversal), and when the undrained compression begins $(\boldsymbol{\alpha} - \boldsymbol{\alpha}_{in}) : \boldsymbol{n} > 0$, the plastic modulus K_p remains a positive and finite value, without

minimizing the plastic strain increment during the first step. This is why in Method 2, during undrained compression, the slope of the stress path in Figure 15d starts immediately inclined, a decrease in mean effective stress initiates from the first stem and the simulated instability stress ratio is lower than the one predicted in Method 1. On the other hand, during undrained extension with Method 2, $(\boldsymbol{\alpha} - \boldsymbol{\alpha}_{in}) : \boldsymbol{n} < 0$, $\boldsymbol{\alpha}_{in} = 0$, $\boldsymbol{\alpha}$ is a compression-like tensor due to a compression consolidation process and $\boldsymbol{n}$ is an extension-like tension. This updates $\boldsymbol{\alpha}_{in}$, a new loading process initiates and the response is elastic for the first few steps due to the very large plastic modulus.

Even though Method 1 has been used in the literature before (e.g., Najma and Latifi (2017)), the update in $\boldsymbol{\alpha}_{in}$ for both the compression and extension cases means that the loading history during consolidation affects equally the two cases by indicating that a new loading process begins. We believe that Method 2 should be preferred since it reflects more realistically the conditions experienced in the laboratory and takes into account the effect of loading history. Thus, we adopt Method 2 to investigate the effect of initial anisotropic consolidation on the onset of instability. Figure 16 shows the results of simulations of triaxial compression and extension responses for several anisotropic consolidation ratios, K_c ranging from 0.4 to 1.6 at void ratio 0.915 and mean effective confining stress of 100kPa. Note that consolidation ratios of $K_c = 1.0$, $K_c < 1.0$ and $K_c > 1.0$ represent specimens that are isotropically, compressionally, and extensionally consolidated, respectively. The undrained triaxial compression tests (see Figure 16a,b) show that as K_c decreases, it is easier to trigger an instability. For instance, in the case of $K_c = 0.4$, there is a spontaneous collapse (that is, decreasing deviatoric stress with increasing axial strain), also referred to as "incipient instability" (Buscarnera and Whittle, 2013). A similar behavior is observed in the triaxial extension tests (see Figure 16c,d), but now it is easier to trigger liquefaction as K_c increases. In this case, the incipient instability is observed at a consolidation ratio K_c of 1.5 or higher.

Using the results from Figure 16, Figure 17 shows that anisotropic consolidated specimens have a higher instability stress ratio (η_f) in triaxial compression than in triaxial extension. In undrained triaxial compression tests on extensionally consolidated samples, it is observed that the instability stress-ratio gradually decreases as the anisotropy in consoli-

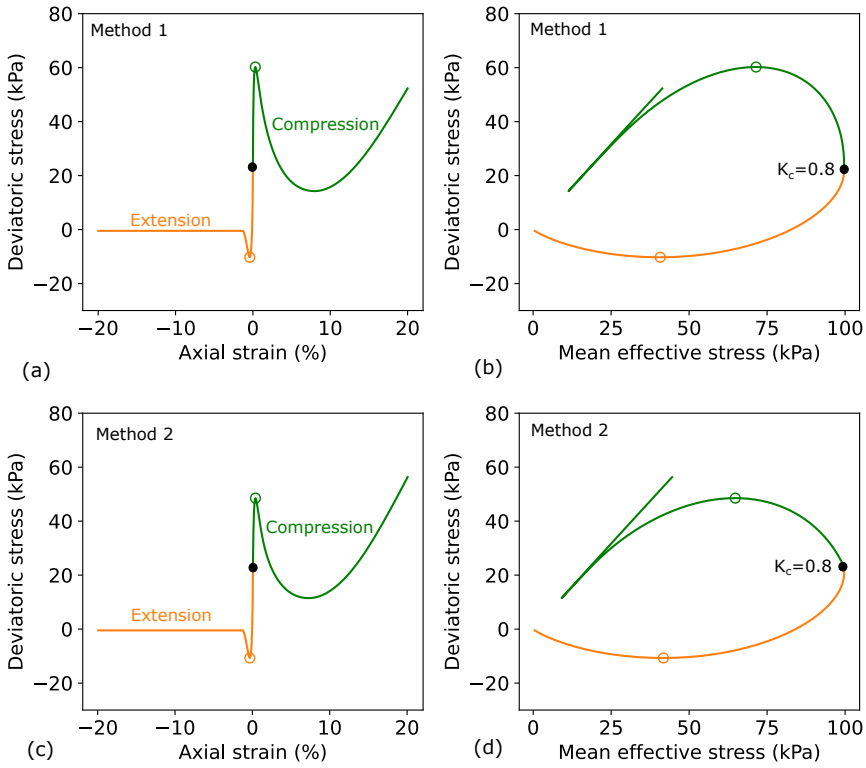

Figure 15: Constitutive responses in triaxial compression and extension using Method 1 (a, b) and using Method 2 (c, d).

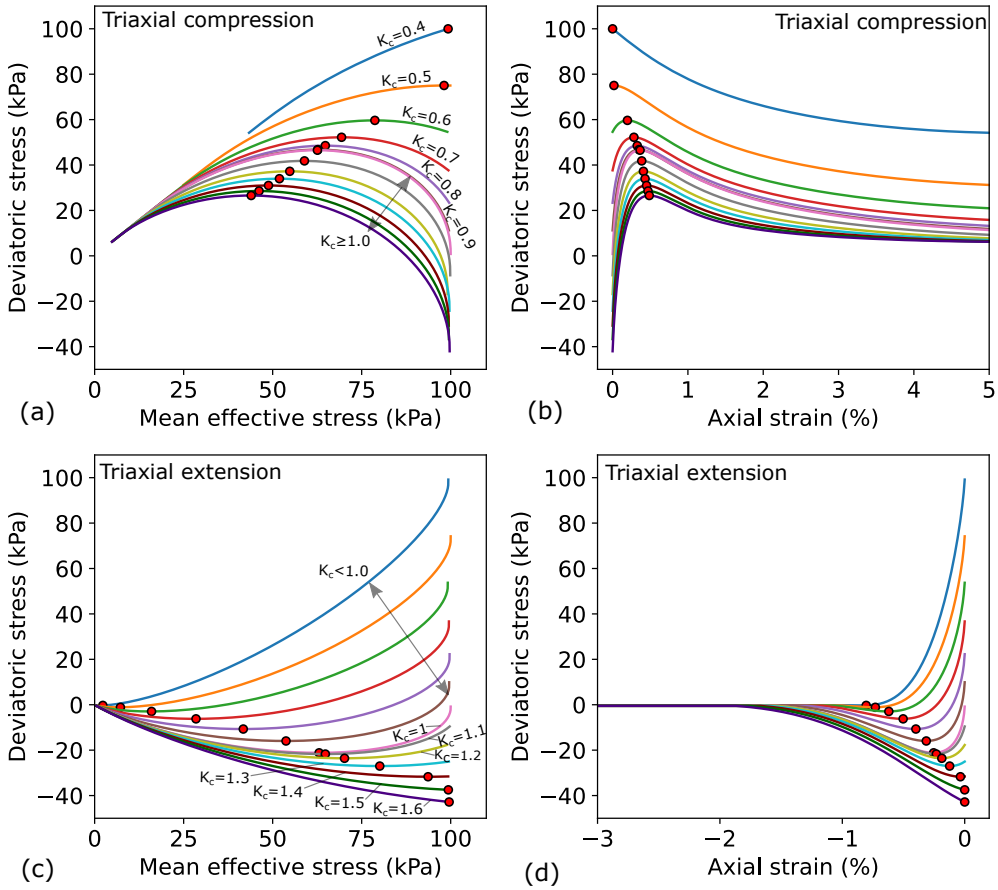

Figure 16: Constitutive responses for several anisotropically consolidated specimens with K_c ranging from 0.4 to 1.6 in triaxial compression (a, b) and triaxial extension (c, d).

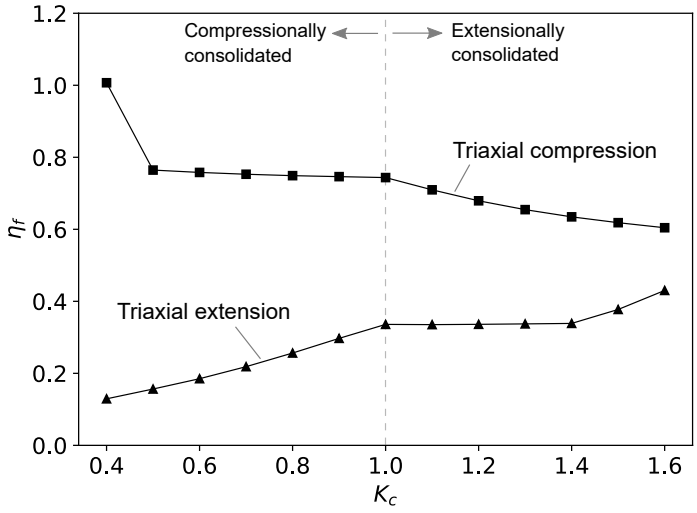

Figure 17: Variation of instability stress ratio with respect to initial consolidation ratio, K_c, for triaxial compression and triaxial extension.

dation increases (i.e., increase in K_c). But, from the undrained triaxial compression tests on compressional consolidated specimens, it is observed that the initial consolidation ratio has no significant effect on the stress ratio at the instability point except for extreme K_c values; where due to the immediate collapse behavior, there is an increase in instability stress ratio for K_c values < 0.5. Similar observations hold for the undrained triaxial extension tests where the compressional consolidated specimens show a decrease in instability stress ratio with the increase in anisotropic consolidation (i.e., decrease in K_c) and extensionally consolidated specimens have no significant effect on the instability stress ratio except for extreme K_c values (> 1.4). The results presented for the triaxial compression tests on compressional consolidated specimens in Figures 16 and 17 are consistent with previous experimental studies (Chu and Wanatowski, 2008; Kato et al., 2001; Yang et al., 2021).

8. Discussion

All the numerical simulations in this study were performed with the fabric based SANISAND-F constitutive model, implemented in a strain-driver algorithm proposed in Bardet and Choucair (1991), that assumes homogeonous stress and strain field within a Representative

Elementary Volume (REV). This is consistent with previous efforts that also focused on the material point response (Andrade, 2009; Borja, 2006; Najma and Latifi, 2017); however, in contrast to these previous studies, we used the ACST framework that allows incorporating fabric anisotropy effects as highlighted in Section 1. Gao and Zhao (2013) demonstrated the effect of fabric anisotropy on the triggering and evolution of localized deformation, when dilative granular soils are loaded in drained conditions (strain localization), by treating the deformation of the REV as a boundary value problem using the Finite Element Method. In this study the effect of fabric anisotropy on dilatancy, and thus, on the rate of pore pressure generation during undrained loading was examined as the dominant mechanism of liquefaction triggering, assuming diffused instability (Borja, 2006; Darve, 1996; Wu et al., 2020), with no account for localized deformation. Future research could be done to investigate the effect of localized deformation on liquefaction triggering in loose contractive sands under undrained loading by treating the deformation of the REV as a boundary value problem and using fabric-based models with appropriate numerical methods for mesh-dependent solutions (e.g. Gao et al. (2021); Jirasek (1998); Mallikarachchi and Soga (2020)).

We would also like to highlight the need for more experimental studies on the quantification of the initial microstructure associated with different reconstitution methods, considering the evolution of fabric under multiple loading paths during deformation –in line with recent studies (Viggiani and Tengattini, 2019; Zhao et al., 2021). These studies would be instrumental to enable further validation of the trends presented in Section 5 (effect of initial fabric). Lastly, we want to emphasize that our study was focused on the triggering of liquefaction instability, a useful concept for estimating liquefaction trigerring in engineering practice (Boulanger and Idriss, 2016; Robertson, 2010; Saye et al., 2021), however, it did not include post-triggering deformation analysis, which could be considered in future studies.

9. Conclusions

In this study, we have used the SANISAND-F model formulated under the ACST framework to investigate the flow liquefaction triggering in sands under undrained loading conditions, considering the role of state, multiaxial loading and fabric anisotropy. It was shown

that the ACST framework provides benefits to account for generalized loading and fabric effects. In this context, we derived criteria that predict instability conditions for generalized undrained loading including anisotropy and fabric effects. An interesting finding is that the instability surface constructed using the derived criteria is not hexagonally symmetrical with respect to the origin in the stress space. This is due to the fact that within the ACST framework, the relative effects of soil fabric and the loading direction are taken into account in the estimation of the instability stress ratios. Thus, the resistance to flow liquefaction (represented as the distance between the origin and the instability surface) changes as a function of the Lode angle and fabric anisotropy. In agreement with with experimental results, the instability stress ratios estimated from the derived instability criteria are dependent on b and α_σ and can also be significantly influenced by the initial fabric, which highlights coupling effects between the loading and fabric evolution. For example, the onset of instability for a given Lode angle and an increasing α_σ can be promoted or not, depending on the interactions between the loading and fabric directions. We also showed that there is no significant evolution of the state variables that control the instability stress ratio from initial to instability conditions. This provides a practical means to derive instability stress ratios for generalized loading conditions once the SANISAND-F parameters (often calibrated for triaxial conditions) and the values of initial state variables are known. Lastly, the different strategies for estimating instability stress ratios when the undrained loading is imposed after an initial anisotropic consolidation were discussed. Unless there is evidence of loading/unloading processes that update the value of $\boldsymbol{\alpha}_{in}$, we recommend using a two step process that consists of simulating anisotropic consolidation before imposing the undrained loading boundary conditions (i.e., $\boldsymbol{\alpha}_{in}$ is updated only upon loading reversal). We showed that this strategy provides results that are consistent with previous experimental studies in triaxial compression conditions, where the instability stress ratio is not significantly affected by the initial anisotropic consolidation before loading.

Acknowledgements

This study has been funded by the National Science Foundation (NSF) under the CMMI 2013947 project.

References

Andrade, J.E., 2009. A predictive framework for liquefaction instability. Géotechnique 59, 673–682.

Andrade, J.E., Ramos, A.M., Lizcano, A., 2013. Criterion for flow liquefaction instability. Acta Geotechnica 8, 525–535.

Bardet, J.P., Choucair, W., 1991. A linearized integration technique for incremental constitutive equations. International Journal for Numerical and Analytical Methods in Geomechanics 15, 1–19. doi:10.1002/nag.1610150102.

Been, K., Jefferies, M., 2004. Stress dilatancy in very loose sand. Canadian Geotechnical Journal 41, 972–989.

Been, K., Jefferies, M.G., 1985. A state parameter for sands. Géotechnique 35, 99–112.

Bjerrum, L., 1971. Subaqueous slope failures in norwegian fjords. Norwegian Geotechnical Institute Publ .

Borja, R.I., 2006. Condition for liquefaction instability in fluid-saturated granular soils. Acta Geotechnica 1, 211.

Buscarnera, G., Whittle, A.J., 2012. Constitutive modelling approach for evaluating the triggering of flow slides. Canadian Geotechnical Journal 49, 499–511.

Buscarnera, G., Whittle, A.J., 2013. Model prediction of static liquefaction: influence of the initial state on potential instabilities. Journal of Geotechnical and Geoenvironmental Engineering 139, 420–432.

Castro, G., 1969. Liquefaction of sands. ph. D. Thesis, Harvard Soil Mech. .

Chu, J., Leroueil, S., Leong, W.K., 2003. Unstable behaviour of sand and its implication for slope instability. Canadian Geotechnical Journal 40, 873–885.

Chu, J., Wanatowski, D., 2008. Instability conditions of loose sand in plane strain. Journal of Geotechnical and Geoenvironmental Engineering 134, 136–142.

Dafalias, Y.F., Manzari, M.T., 2004. Simple Plasticity Sand Model Accounting for Fabric Change Effects. Journal of Engineering Mechanics 130, 622–634.

Dafalias, Y.F., Papadimitriou, A.G., Li, X.S., 2004. Sand plasticity model accounting for inherent fabric anisotropy. Journal of Engineering Mechanics 130, 1319–1333.

Darve, F., 1996. Liquefaction phenomenon of granular materials and constitutive stability. Engineering computations .

Fourie, A., Blight, G., Papageorgiou, G., 2001. Static liquefaction as a possible explanation for the merriespruit tailings dam failure. Canadian Geotechnical Journal 38, 707–719.

Gao, Z., Li, X., Lu, D., 2021. Nonlocal regularization of an anisotropic critical state model for sand. Acta Geotechnica , 1–13.

Gao, Z., Zhao, J., 2013. Strain localization and fabric evolution in sand. International Journal of Solids and Structures 50, 3634–3648.

Gao, Z., Zhao, J., 2015. Constitutive modeling of anisotropic sand behavior in monotonic and cyclic loading. Journal of Engineering Mechanics 141, 04015017.

Gao, Z., Zhao, J., Li, X.S., Dafalias, Y.F., 2014. A critical state sand plasticity model accounting for fabric evolution. International journal for numerical and analytical methods in geomechanics 38, 370–390.

Georgiannou, V.N., Tsomokos, A., 2008. Comparison of two fine sands under torsional loading. Canadian Geotechnical Journal 45, 1659–1672.

Hazen, A., 1918. A study of the slip in the calaveras dam. Engineering News Record 81, 1158–1164.

Hill, R., 1958. A general theory of uniqueness and stability in elastic-plastic solids. Journal of the Mechanics and Physics of Solids 6, 236–249.

Ishihara, K., 1993. Liquefaction and flow failure during earthquakes. Geotechnique 43, 351–451.

Ishihara, K., 1996. Soil Behaviour in Earthquake Geotechnics. Oxford engineering science series, Clarendon Press.

Jefferies, M., Been, K., 2019. Soil liquefaction: a critical state approach. CRC press.

Jefferies, M.G., 1993. Nor-Sand: a simle critical state model for sand. Géotechnique 43, 91–103.

Jirasek, M., 1998. Nonlocal models for damage and fracture: comparison of approaches. International Journal of Solids and Structures 35, 4133–4145.

Kato, S., Ishihara, K., Towhata, I., 2001. Undrained shear characteristics of saturated sand under anisotropic consolidation. Soils and Foundations 41, 1–11.

Konrad, J.M., 1993. Undrained response of loosely compacted sands during monotonic and cyclic compression tests. Géotechnique 43, 69–89.

Kramer, S.L., 1996. Geotechnical earthquake engineering. Pearson Education India.

Lade, P.V., 1992. Static instability and liquefaction of loose fine sandy slopes. Journal of Geotechnical Engineering 118, 51–71.

Lade, P.V., 1993. Initiation of static instability in the submarine Nerlerk berm. Canadian Geotechnical Journal 30, 895–904.

Lade, P.V., 1999. Instability of granular materials, in: Physics and mechanics of soil liquefaction. Rotterdam: Balkema, pp. 3–16.

Lashkari, A., 2016. Prediction of flow liquefaction instability of clean and silty sands. Acta Geotechnica 11,

987–1014.

Leguizamón-Barreto, L.C., Ramos-Cañón, A.M., Andrade, J.E., 2021. Undrained instability detection under general stress conditions. Acta Geotechnica , 1–19.

Li, X.S., Dafalias, Y.F., 2012. Anisotropic critical state theory: role of fabric. Journal of Engineering Mechanics 138, 263–275.

Lü, X., Huang, M., Andrade, J.E., 2017. Predicting the initiation of static liquefaction of cross-anisotropic sands under multiaxial stress conditions. International Journal for Numerical and Analytical Methods in Geomechanics 41, 1724–1740.

Mallikarachchi, H., Soga, K., 2020. Post-localisation analysis of drained and undrained dense sand with a nonlocal critical state model. Computers and Geotechnics 124, 103572.

Manzari, M.T., Dafalias, Y.F., 1997. A critical state two-surface plasticity model for sands. Geotechnique 47, 255–272.

Miura, S., Toki, S., 1982. A sample preparation method and its effect on static and cyclic deformation-strength properties of sand. Soils and foundations 22, 61–77.

Mohammadnejad, T., Andrade, J.E., 2015. Flow liquefaction instability prediction using finite elements. Acta Geotechnica 10, 83–100.

Morgenstern, N., Vick, S., Van Zyl, D., 2015. Report on mount polley tailings storage facility breach: Independent expert engineering investigation and review panel. Retrieved from Mount Polley Review Panel website: https://www. mountpolleyreviewpanel. ca/sites/default/files/report/ReportonMountPolleyTailingsStorageFacilityBreach. pdf .

Morgenstern, N., Vick, S., Viotti, C., Watts, B., 2016. Report on the immediate causes of the failure of the fundão dam. Fundão Tailings Dam Review Panel .

Muhammad, K., 2012. Case history-based analysis of liquefaction in sloping ground. University of Illinois at Urbana-Champaign.

Najma, A., Latifi, M., 2017. Analytical definition of collapse surface in multiaxial space as a criterion for flow liquefaction occurrence. Computers and Geotechnics 90, 120–132.

Najma, A., Latifi, M., 2018. Collapse surface approach as a criterion of flow liquefaction occurrence in 3D FEM models. Soil Dynamics and Earthquake Engineering 107, 164–178.

Olson, S.M., 2001. Liquefaction analysis of level and sloping ground using field case histories and penetration resistance. University of Illinois at Urbana-Champaign.

Petalas, A.L., Dafalias, Y.F., Papadimitriou, A.G., 2020. SANISAND-F: Sand constitutive model with evolving fabric anisotropy. International Journal of Solids and Structures 188, 12–31.

Sadrekarimi, A., 2014. Effect of the mode of shear on static liquefaction analysis. Journal of Geotechnical and Geoenvironmental Engineering 140, 04014069.

Salimi, M., Lashkari, A., 2020. Undrained true triaxial response of initially anisotropic particulate assemblies using cfm-dem. Computers and Geotechnics 124, 103509.

Sivathayalan, S., Vaid, Y.P., 2002. Influence of generalized initial state and principal stress rotation on the undrained response of sands. Canadian Geotechnical Journal 39, 63–76.

Sladen, J.A., D'hollander, R.D., Krahn, J., Mitchell, D.E., 1985. Back analysis of the Nerlerk berm liquefaction slides. Canadian Geotechnical Journal 22, 579–588.

Sze, H., Yang, J., 2014. Failure modes of sand in undrained cyclic loading: impact of sample preparation. Journal of geotechnical and geoenvironmental engineering 140, 152–169.

Tatsuoka, F., Ochi, K., Fujii, S., Okamoto, M., 1986. Cyclic undrained triaxial and torsional shear strength of sands for different sample preparation methods. Soils and Foundations 26, 23–41.

Theocharis, A.I., Vairaktaris, E., Dafalias, Y.F., Papadimitriou, A.G., 2017. Proof of incompleteness of critical state theory in granular mechanics and its remedy. Journal of Engineering Mechanics 143, 4016117.

Uthayakumar, M., Vaid, Y.P., 1998. Static liquefaction of sands under multiaxial loading. Canadian Geotechnical Journal 35, 273–283.

Vaid, Y.P., Sivathayalan, S., Stedman, D., 1999. Influence of specimen-reconstituting method on the undrained response of sand. Geotechnical Testing Journal 22, 187–195.

Verdugo, R., Ishihara, K., 1996. The steady state of sandy soils. Soils and foundations 36, 81–91.

Viggiani, G., Tengattini, A., 2019. Recent developments in laboratory testing of geomaterials with emphasis on imaging. Proceedings of the XVII ECSMGE-2019 Reykjavík, Iceland 9, 2019.

Wang, R., Dafalias, Y.F., Fu, P., Zhang, J.M., 2020. Fabric evolution and dilatancy within anisotropic critical state theory guided and validated by DEM. International Journal of Solids and Structures 188, 210–222.

Wu, Q., Xu, T., Yang, Z., 2020. Diffuse instability of granular material under various drainage conditions: discrete element simulation and constitutive modeling. Acta Geotechnica 15, 1763–1778.

Yang, J., Liang, L.B., Chen, Y., 2021. Instability and liquefaction flow slide of granular soils: the role of initial shear stress. Acta Geotechnica , 1–15.

Yang, Z.X., Li, X.S., Yang, J., 2008. Quantifying and modelling fabric anisotropy of granular soils. Géotechnique 58, 237–248.

Yoshimine, M., Ishihara, K., Vargas, W., 1998. Effects of principal stress direction and intermediate principal stress on undrained shear behavior of sand. Soils and Foundations 38, 179–188.

Zhao, C.F., Pinzón, G., Wiebicke, M., Andò, E., Kruyt, N.P., Viggiani, G., 2021. Evolution of fabric anisotropy of granular soils: X-ray tomography measurements and theoretical modelling. Computers and Geotechnics 133, 104046.